nature communications

Article

https://doi.org/10.1038/s41467-024-51499-z

Single-photon induced instabilities in a cavity electromechanical device

Received: 28 September 2023

Accepted: 9 August 2024

Published online: 19 August 2024

Check for updates

Tanmoy Bera[1] ✉, Mridul Kandpal[1], Girish S. Agarwal[1,2,3,4] & Vibhor Singh[1] ✉

Cavity-electromechanical systems are extensively used for sensing and controlling the vibrations of mechanical resonators down to their quantum limit. The nonlinear radiation-pressure interaction in these systems could result in an unstable response of the mechanical resonator showing features such as frequency-combs, period-doubling bifurcations and chaos. However, due to weak light-matter interaction, typically these effects appear at very high driving strengths. By using polariton modes formed by a strongly coupled flux-tunable transmon and a microwave cavity, here we demonstrate an electromechanical device and achieve a single-photon coupling rate $(g_0/2\pi)$ of 160 kHz, which is nearly 4% of the mechanical frequency ω_m. Due to large g_0/ω_m ratio, the device shows an unstable mechanical response resulting in frequency combs in sub-single photon limit. We systematically investigate the boundary of the unstable response and identify two important regimes governed by the optomechanical backaction and the nonlinearity of the electromagnetic mode. Such an improvement in the single-photon coupling rate and the observations of microwave frequency combs at single-photon levels may have applications in the quantum control of the motional states and critical parametric sensing. Our experiments strongly suggest the requirement of newer approaches to understand instabilities.

Light carries momentum, and it can be used to control and manipulate the motion of a mechanical resonator down the quantum regime[1]. Such control over the motional states is essential for technological advancement as well as to probe the fundamental physics[2,3]. In cavity-electromechanical devices, two linear modes, namely an electromagnetic (EM) mode and a mechanical mode are coupled with the nonlinear radiation-pressure interaction[1,4]. In the microwave domain, the vibrations of the mechanical resonators are typically integrated into the EM mode using charge modulation[5–13]. Recently, cavity electromechanical devices utilizing the magnetic-flux modulation of Josephson inductance have shown interesting results such as large electromechanical coupling rates[14–17], the near-ground state cooling of the mechanical resonator by four-wave-mixing[18], and Kerr-enhanced techniques[19]. Further, such devices have been proposed to reach the single-photon strong coupling regime using its linear scaling with the magnetic field[20–22].

Apart from providing the electromechanical coupling, the nonlinear nature of the Josephson inductance in flux-coupled electromechanical systems can be a valuable resource[18,19]. It allows us to control the nature of the electromagnetic mode to change from the weak-Kerr to a single photon strong-Kerr oscillator where the response remains nonlinear down to a single excitation. Further, under certain control parameters, the electromagnetic (EM) mode can made to undergo a dissipative phase transition with strong fluctuations in the photon number[23]. Therefore, coupling a mechanical resonator to such an EM mode using radiation-pressure interaction offers a unique platform to study and discern the effects stemming from the nonlinear nature of the radiation-pressure interaction[13,24],

[1]Department of Physics, Indian Institute of Science, Bangalore 560012, India. [2]Institute for Quantum Science and Engineering, Texas A&M University, College Station, TX 77843, USA. [3]Department of Physics and Astronomy, Texas A&M University, College Station, TX 77843, USA. [4]Department of Biological and Agricultural Engineering, Texas A&M University, College Station, TX 77843, USA. ✉e-mail: btanmoy@iisc.ac.in; v.singh@iisc.ac.in

https://doi.org/10.1038/s41467-024-51499-z

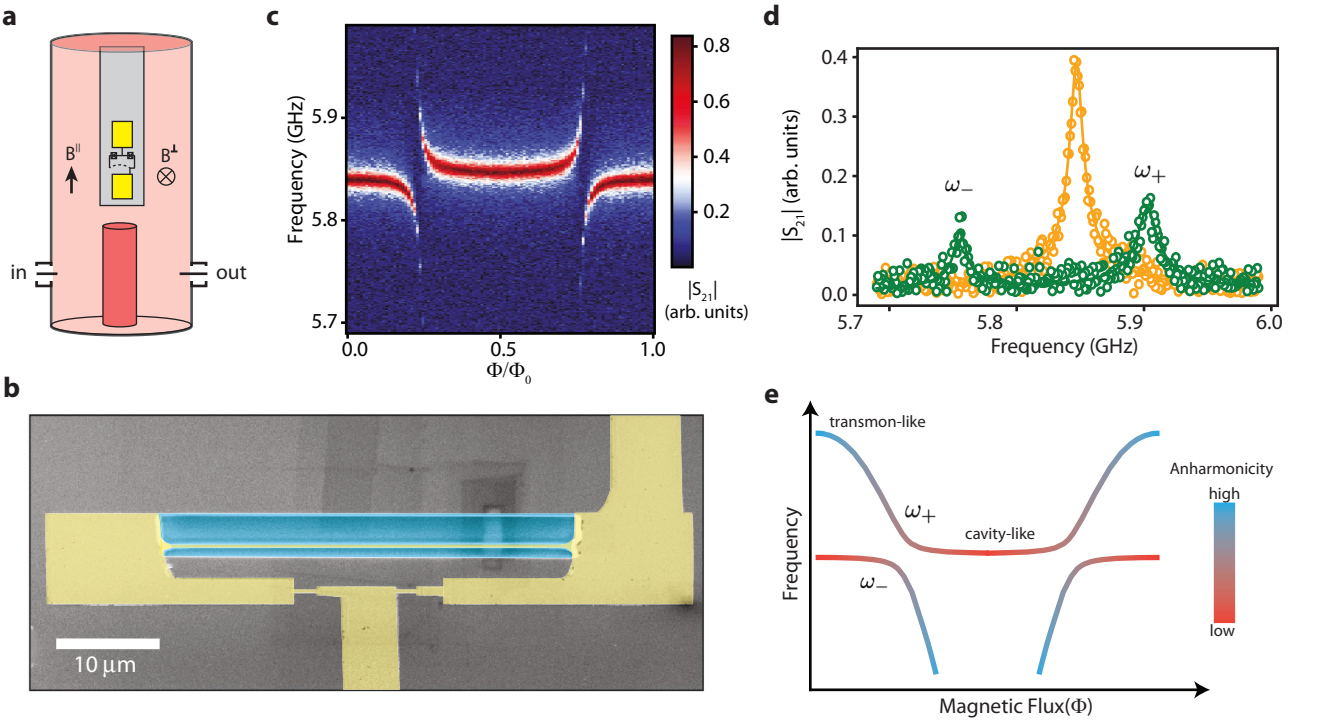

Fig. 1 | Concept. a A schematic of a quarter wavelength coaxial cavity (red) coupled to a transmon (yellow). The two pads provide the shunting capacitance as well as coupling capacitance to the cavity. The axial and normal components of the magnetic field are denoted by $B^{\parallel}$ and $B^{\perp}$, respectively. **b** A tilted false-color scanning electron microscope image of the SQUID loop with embedded mechanical resonator. The suspended Al nanomechanical resonator can be seen. The Al film and the silicon substrate are shown in yellow and gray colors, respectively. The selective-etched region used to suspend the mechanical resonator is shown by the cyan-colored region. The mechanical resonator has dimensions of 40 μm × 200 nm × 28 nm. **c** A representative color plot of the voltage transmission $|S_{21}|$ through the cavity as the magnetic flux through the SQUID loop is varied. **d** The panel shows a linecut from panel (**c**), corresponding to $\Phi/\Phi_0 = 0.27(0.5)$ in green (yellow) emphasizing the vacuum-Rabi split peaks (dressed-cavity peak). The solid lines are complex Lorentzian fits and plotted as a guide to the eye. **e** A schematic to depict the change in frequency of the dressed modes as the magnetic flux is swept. The gradual color shift from blue to red or vice versa indicates how the nonlinear character of the mode is changing with flux.

as well as the ones from the nonlinear nature of the electromagnetic mode[23].

Here, we demonstrate an electromechanical device consisting of a linear cavity, a frequency tunable transmon qubit, and a mechanical resonator[15]. First, the flux-tunability of the transmon qubit is used to implement the electromechanical coupling. Second, tuning of the transmon frequency in resonance with the cavity forms the new eigenstates due to the designed strong coupling. The anharmonicity of the resultant polariton modes can be controlled by transmon-cavity detuning[25,26]. Such a tri-partite system thus allows us to control the electromechanical coupling and the nonlinearity of the EM mode in a single device. Therefore, by controlling the strength of the nonlinearity, the electromechanical effects can be explored as the EM mode undergoes various regimes such as super-splitting, multi-photon transitions[25,27], critical slowing down[28], photon blockade breakdown[29,30], and transmon-ionization[31].

Results

Device concept

The frequency tunable transmon qubit is enabled by a SQUID loop and a capacitor. Figure 1a shows the schematic design of the device. The coaxial cavity is placed inside a 2-axis vector magnet, allowing us to control the axial and the normal components of the magnetic field independently. The cavity is machined from oxygen-free high conductivity (OHFC) copper. The transmon qubit is fabricated on an intrinsic-Si chip using electron beam lithography and shadow evaporation of aluminum. To achieve a larger critical in-plane magnetic field, we use 28 nm thin Al film to fabricate the device[32]. The mechanical resonator is realized by suspending one of the arms of the SQUID loop by selective isotropic dry etching of the silicon substrate. The transmon frequency can be tuned by varying the magnetic flux through the SQUID loop.

A false color scanning electron microscope image of the SQUID loop with the suspended mechanical resonator is shown in Fig. 1b. The patterned chip is placed inside the coaxial cavity and cooled down to 20 mK in a dilution refrigerator. The details of device fabrication, and measurement setup are given in Supplementary Note 1. Since superconducting films show more resilience to the in-plane magnetic field[32], we focus on the electromechanical coupling of the out-of-plane vibrational mode of the mechanical resonator. Further, by using the control over the normal component of the magnetic field, we can cancel any out-of-plane component of the magnetic field arising from the misalignment between the axial field and SQUID plane.

Measurements

We report measurements from two similar devices but with substantially different transmon-cavity coupling rates. Detailed parameters for both the devices are listed in Supplementary Note 2. We first begin by measuring the voltage transmission $|S_{21}(\omega)|$ of Device-1 through the cavity while varying the magnetic flux through the SQUID loop. Depending on the flux passing through the SQUID loop, the transmon frequency can vary from its maximum value to a minimum value. Figure 1c shows the color plot of the cavity transmission. As the transmon is brought in resonance with the cavity, the measured transmission splits into two well-separated dressed modes as shown in Fig. 1d, demonstrating the strong coupling. Provided low strength of the input power, the dressed cavity mode for $\Phi/\Phi_0 = 0.5$, and the vacuum Rabi-split peaks (VRS) for $\Phi/\Phi_0 = 0.27$ have the characteristic

https://doi.org/10.1038/s41467-024-51499-z

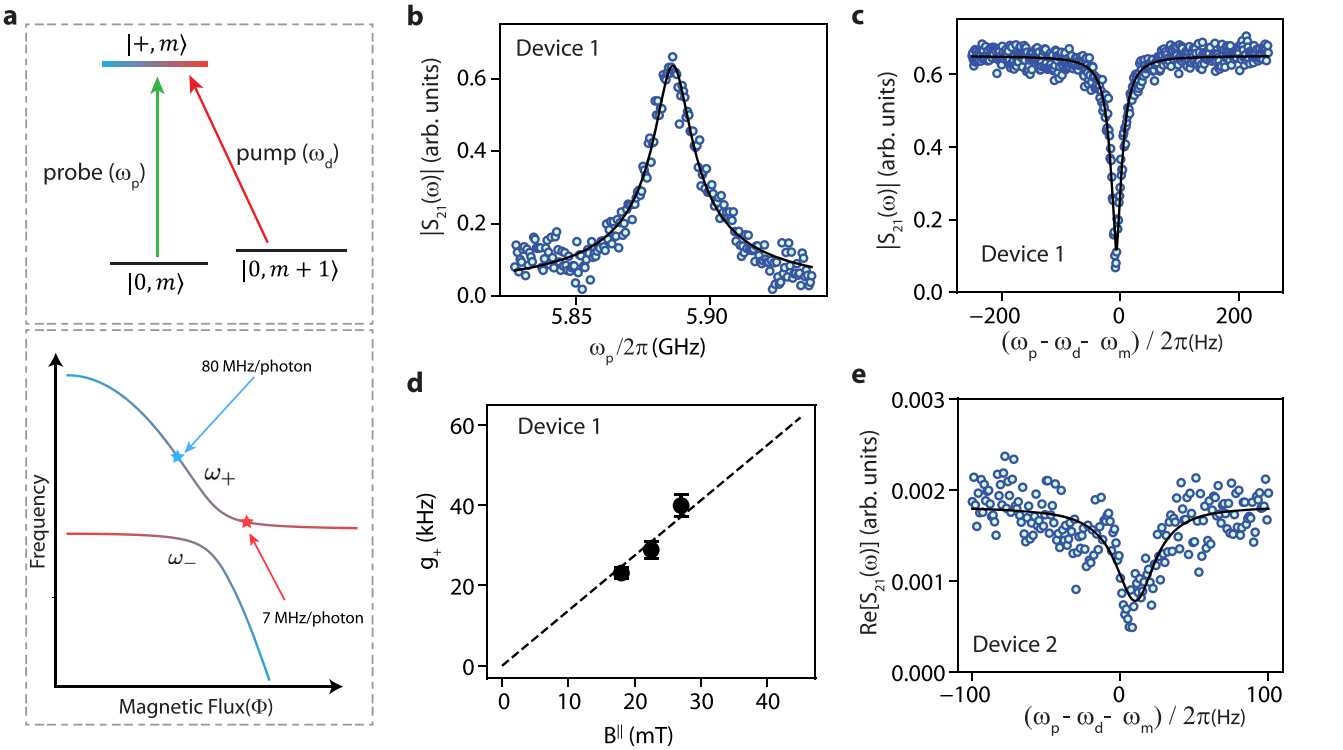

Fig. 2 | Cavity-enabled qubit-phonon absorption (CEQA). a The top panel depicts the pump (shown in red) and probe (shown in green) scheme for the CEQA experiment. The states $|+,m\rangle$ denote one excitation in the polariton mode, along with m excitations in the mechanical resonator. The lower panel schematically illustrates operating points for the CEQA experiment in both devices. The red star represents the operating point in Device-1, indicating weak nonlinearity in the polariton mode. The blue star represents the operating point in Device-2, indicating strong nonlinearity. **b** Measurement of $|S_{21}|$ in the absence of the pump signal, showing the linear response of the polariton mode. The solid-black line is a Lorentzian fit to the response. **c** In the presence of a pump signal, an absorption feature appears in the probe transmission. At $B^{\parallel}$ ~ 27 mT, the polariton mode frequency is set to $\omega_+/2\pi$ ~ 5.884 GHz. The applied pump strength is $P_i = -19$ dBm, which corresponds to mean photon occupation of $(5.80 \pm 0.07) \times 10^{-2}$, and the probe signal is 6 dB smaller than the pump. The solid black curve is the fitted curve yielding a single-photon coupling rate $g_+/2\pi$ ~ 40.0 ± 5.5 kHz. **d** Experimentally determined g_+ for three different values of the applied magnetic field $B_{\parallel}$. While increasing $B^{\parallel}$, the flux-responsivity is nominally kept constant by adjusting $B^{\perp}$. The error represents the statistical uncertainty. The dashed line represents a linear fit. **e** The absorption feature arising in the probe transmission of a strongly nonlinear mode in Device-2. The mode frequency is chosen to be $\omega_+/2\pi$ ~ 6.005 GHz, which corresponds to a qubit detuning of $(\omega_q - \omega_c)/2\pi \sim 120$ MHz. An analytical formula derived for a two-level system coupled to a mechanical resonator is used to fit the data, yielding the solid black curve.

Lorentzian lineshape. From the separation of VRS, we infer the strength of the transmon-cavity coupling to be 72 MHz. The reduction in the peak height of VRS in resonant conditions suggests that energy dissipation via the transmon qubit dominates over the cavity dissipation rate.

In the resonant limit of transmon-cavity, it is suitable to describe the system in terms of new eigenstates, denoted by upper and lower polariton modes with frequency ω_+ and ω_-, respectively. Away from the resonant limit, these modes exhibit a cavity-like or a transmon-like behavior with distinct anharmonicity as represented by the gradual change of color in Fig. 1e. These polariton modes retain the flux tunability due to underlying SQUID inductance, allowing them to be utilized for implementing electromechanical interaction. Further, due to the large spectral separation between the two modes, we can analyze and describe each mode's optomechanical effect separately. Considering the upper mode, the Hamiltonian of the tri-partite system can be reduced to

$$H \simeq \omega_+ \hat{a}_+^\dagger \hat{a}_+ - \frac{K_+}{2}\left(\hat{a}_+^\dagger \hat{a}_+\right)^2 + g_+ \hat{a}_+^\dagger \hat{a}_+ \left(\hat{b} + \hat{b}^\dagger\right) + \omega_m b^\dagger b, \quad (1)$$

where ω_+, K_+, ω_m, and g_+ are the upper mode frequency, Kerr nonlinearity, mechanical mode frequency, and single-photon electromechanical coupling rate, respectively. The ladder operators of the upper polariton mode and the mechanical mode are denoted by $\hat{a}_+ (\hat{a}_+^\dagger)$ and $\hat{b}(\hat{b}^\dagger)$, respectively. The single-photon electromechanical coupling rate of the upper polariton mode can be expressed as $g_+ \simeq \xi G_+ B^{\parallel} l x_{zp}$, where $G_+ = d\omega_+/d\Phi$ is the flux responsivity of the upper polariton mode, $B^{\parallel}$ is the axial component of the applied magnetic field, l is the length of the mechanical resonator, x_{zp} is the quantum zero-point fluctuations of the mechanical resonator, and ξ is a geometrical factor of order unity and depends on the mechanical mode-shape. It is evident that a higher single-photon electromechanical coupling rate can be achieved by increasing the flux-responsivity G_+ and magnetic field $B^{\parallel}$. However, the increased flux-responsivity of the dressed mode comes at the cost of reduced transmission. For the experiments discussed in the next section, we choose an operating frequency ω_+ in Device-1 that is 20–80 MHz detuned from the bare cavity frequency.

Cavity-enabled qubit-phonon absorption

To probe the electromechanical coupling, we use a pump–probe scheme, similar to the electromagnetically induced transparency technique[33,34]. Figure 2a shows the schematic of the different transitions involved in the measurement. Two coherent signals are sent to the device, i.e., a pump signal at a red detuned frequency $(\omega_+ - \omega_m)$ which drives the $|0, m+1\rangle \leftrightarrow |+, m\rangle$ transition, and a weak probe signal at ω_p (near ω_+) to measure the transmission. We emphasize that due to the tunable nature of the polariton modes in our device, we can carry out such experiments in both low and strong anharmonicity limits, as shown in the lower panel of Fig. 2a.

We first perform the experiment in Device-1 with a cavity-like mode. Without the pump, the voltage transmission $|S_{21}(\omega_p)|$ shows the characteristic Lorentzian lineshape, as shown in Fig. 2b. In the presence of the pump, an absorption feature appears in the transmission spectrum, as shown in Fig. 2c. It arises from the destructive interference of the probe field from two different pathways[35]. The shape of the absorption feature is determined by the response of the mechanical resonator and can be used to extract its resonant frequency and effective dissipation rate. From these measurements, we obtain the mechanical resonant frequency and linewidth to be $\omega_m/2\pi$ ~3.97 MHz and ~13 Hz, respectively. In addition, we determine the single-photon coupling strength g_+ by fitting the absorption feature with an analytical expression calculated by treating the electromagnetic mode as an anharmonic oscillator (Supplementary Note 3). We repeat the experiment for various pump strengths and extract the electromechanical coupling strength $g_+/2\pi$ ~ 40.0 ± 2.7 kHz, with uncertainty arising from the statistical measurements. Since the single-photon electromechanical coupling rate is linearly proportional to the axial magnetic field $B^{\parallel}$, we carry out similar absorption experiments at different magnetic fields and calculate the single-photon electromechanical coupling rates. Figure 2d shows the plot of experimentally determined g_+ for different values of the magnetic field.

Next, we utilize the transmon-like mode which exhibits a significantly larger anharmonicity compared to its dissipation rate. These measurements are done on Device-2, which is designed to have a transmon-cavity coupling of $J/2\pi$ ~ 193 MHz. For the three-mode system discussed here, measurement of the transmon−phonon interaction is enabled by the cavity, we call this process cavity-enabled qubit-phonon absorption (CEQA). In the large anharmonicity limit, the absorption feature in probe transmission is shown in Fig. 2e. Due to its large anharmonicity, the CEQA feature effectively arises dominantly from the participation of ground and first excited states of the transmon-like mode. Consequently, we can approximate the electromechanical interaction as an effective two-level system longitudinally coupled to a mechanical resonator. Keeping this in mind, we derive an analytical expression for the absorption feature and fit the experimental data, resulting in the black line shown in Fig. 2e. Additional details pertaining to the calculations are given in Supplementary Note 3. We emphasize that due to large g_+ in the system, the CEQA feature appears in both weak and strong nonlinearity regimes down to the mean-photon occupation of ~10^{-1} and ~10^{-3}, respectively.

Optomechanical backaction and instability

A high single-photon coupling rate results in significant optomechanical backaction at very low pump strengths. To investigate the effects of dynamical backaction on the mechanical resonator, we send a pump signal and measure the power spectral density (PSD) of the output microwave signal while varying the pump power and detuning. Depending on the pump detuning, an imbalance between the up- and down-scattering rates of microwave photons by the mechanical resonator results in its cooling or heating. We first operate at a lower magnetic field of $B^{\parallel}$ ~ 18 mT, and at a mode frequency of $\omega_+/2\pi$ ~ 5.873 GHz, which corresponds to an estimated Kerr nonlinearity of $K_+/2\pi$ ~ 5.1 MHz/photon (see Supplementary Note 2). At such operating frequency, the upper polariton mode has an estimated flux responsivity of $G_+/2\pi$ ~ 1.16 GHz/Φ_0, and expected $g_+/2\pi$ ~ 13.4 ± 0.8 kHz (see Supplementary Note 2). Figure 3a shows the measurements of the effective mechanical linewidth and the shift in the mechanical frequency, extracted from the PSD measurements. As expected, we observe a broadening of the mechanical linewidth for negative detunings and heating and an unstable response for the positive detunings. With the increase in the strength of the pump signal, the backaction effects become enhanced, and the onset of unstable response shifts towards negative detuning due to the Kerr nonlinearity.

To theoretically understand the experimental observation, we model the system as a weak Kerr oscillator with an energy decay rate $\kappa/2\pi$ ~ 14 MHz, estimated from the transmission spectrum. We incorporate the pump by adding a driving term in the effective Hamiltonian given by Eq. (1). To compute the backaction effects on the mechanical resonator, we solve the equations of motion for the coupled modes and obtain the expressions of the effective linewidth Γ_m and the frequency shift $\Delta\omega_m$ of the mechanical resonator (see Supplementary Note 4). The solid black lines in Fig. 3a are the theoretically calculated results.

We next focus on the unstable response of the mechanical resonator. It is defined when the first and second mechanical sideband amplitudes show an abrupt change with the pump power (as shown in Supplementary Fig. 6). Such large vibrational motion of the mechanical resonator produces a prominent frequency comb structure in the PSD with multiple peaks separated by ω_m, as shown in Fig. 3b. In linear cavity optomechanics, such features have been studied extensively, both theoretically and experimentally[1]. We investigate the boundary of the unstable response by varying the pump power and its detuning. Figure 3c shows the results from Device-2, while operating at $\omega_+/2\pi$ ~ 5.82 GHz, corresponding to an energy decay rate of $\kappa/2\pi$ ~ 9 MHz and an electromechanical coupling rate of $g_+/2\pi$ ~ 45.0 ± 1.9 kHz, which is determined from a separate CEQA experiment. It is important to note that due to such a large coupling, the onset of mechanical instability occurs at a mean photon occupation of 0.01 in the polariton mode. To theoretically understand the boundary of the instability, we use a weak-Kerr model as mentioned earlier (Supplementary Note 4). Mechanical instability is defined when the effective mechanical damping rate becomes non-positive. The results from these calculations are shown by the solid-black line in Fig. 3c. By comparing the two theoretical results, we observe that due to the nonlinearity present in the system, the onset of instability shifts toward lower frequencies as the pump power is increased.

Mechanical Instabilities in single-photon strong Kerr limit

We first note that the response of the circuit-QED system can be substantially different at high driving powers. Figure 4a, b shows the cavity transmission $|S_{21}|$ of Device-2 while varying $B^{\perp}$. Apart from the dominating vacuum-Rabi splitting, additional transitions arising from higher levels can also be seen. A schematic of the new (polariton) eigenstates is shown in the right panel of Fig. 4c. The left panel depicts the uncoupled states as $|n_c, n_q\rangle$, where n_c and n_q are the number of excitation in cavity and transmon, respectively. The symmetric and anti-symmetric combination of single excitation states $|1,0\rangle$ and $|0,1\rangle$ are denoted by $|+\rangle$ and $|-\rangle$, respectively. Similarly, the new eigenstates in the two-excitation manifold are labeled as $|\alpha\rangle$, $|\beta\rangle$, and $|\gamma\rangle$. The additional peaks in the transmission spectrum of Fig. 4b are arising from the higher-level transitions, namely $\{|+\rangle, |-\rangle\} \leftrightarrow \{|\alpha\rangle, |\beta\rangle, |\gamma\rangle\}$. Such transitions are possible with a single frequency drive due to non-zero thermal occupation of $|+\rangle$ and $|-\rangle$ states.

To identify these transitions, we treat the transmon as a nonlinear oscillator and model the system using an extended Jaynes−Cummings Hamiltonian added with a coherent drive. We numerically solve the Markovian master equation to compute the voltage transmission. The results are plotted as a solid black line in Fig. 4b. It can be seen that the transition frequencies corresponding to the peaks in the transmission spectrum match closely with the numerical results. Clearly, these transitions arise from the single-photon excitation and are distinct from the multi-photon transitions[25], which usually occur at stronger drive strengths.

We next activate the electromechanical coupling by applying the parallel magnetic field $B^{\parallel}$ ~ 9 mT and investigate the boundary of the unstable response of the mechanical resonator in a wider span of pump power and frequency. Figure 5a, c shows the region of unstable response from Device-2 at two different values of flux-operating point,

https://doi.org/10.1038/s41467-024-51499-z

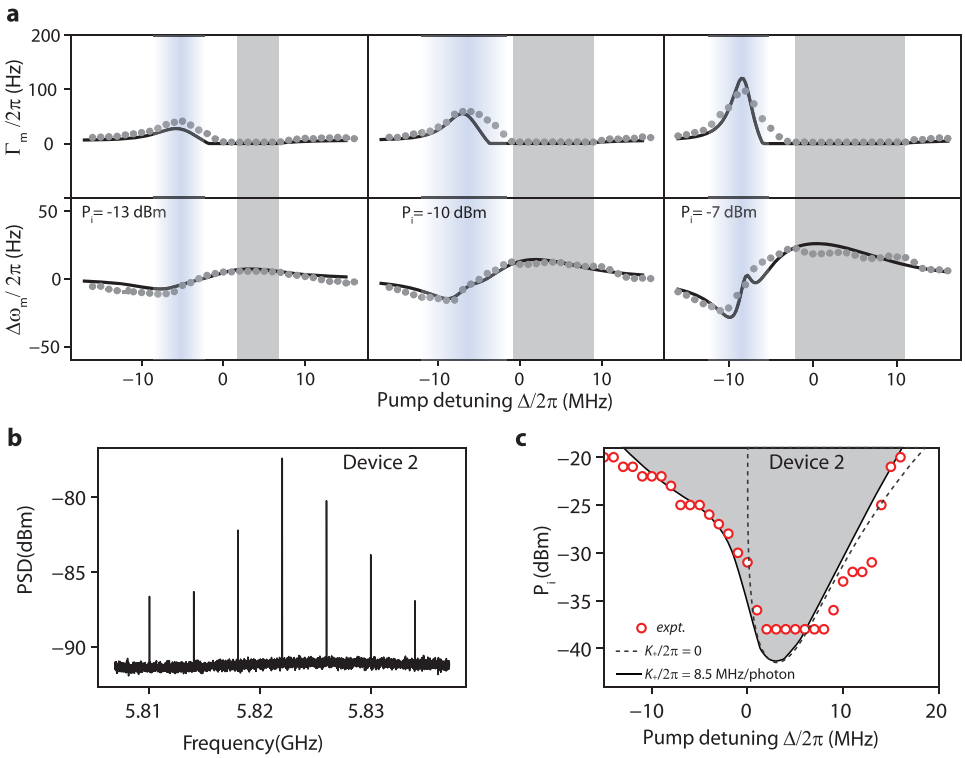

Fig. 3 | Dynamical backaction on the mechanical resonator. a Measurements from Device-1. Total mechanical linewidth and change in the mechanical frequency extracted from the power spectral density (PSD) measurements as the pump detuning is varied at a constant pump power. From left to right panels, the pump power is increased. For these measurements, the dressed mode is tuned to $\omega_+/2\pi$ ~ 5.873 GHz, and the axial magnetic field is set to $B^{\parallel}$ ~ 18 mT, resulting in an electromechanical coupling rate of $g_+/2\pi$ ~ 13.4 ± 0.8 kHz. The solid-black lines are the results of the theoretical calculations based on a Kerr-like oscillator model. The blue-color gradient and gray-shaded region denote the cooling and unstable response of the mechanical resonator. **b** PSD of the output microwave signal showing the formation of the frequency combs separated by ω_m. The measurement is performed using a resolution bandwidth of 5 kHz, pump detuning of $\Delta/2\pi$ ~ 2 MHz, and pump power of −24 dBm. **c** The boundary of the mechanical instability in the parameter space of the pump detuning and power. These measurements are carried out on Device-2 with polariton mode frequency $\omega_+/2\pi$ ~ 5.82 GHz and applied magnetic field $B^{\parallel}$ ~ 9 mT, which resulted in g_+ ~ 45 ± 2.7 kHz. The dashed line is the theoretical prediction based on a linear oscillator model (zero Kerr nonlinearity) with the same electromechanical coupling.

and Fig. 5b, d shows the corresponding transmission spectra at $B^{\parallel} = 0$. For the operating flux in Fig. 5a, the transmon qubit becomes near resonant to the cavity, and the electromechanical coupling rate of the higher frequency polariton mode is estimated to reach $g_+/2\pi$ ~ 160 kHz, which is nearly 4% of the mechanical mode frequency ω_m. As a consequence, the onset of mechanical instability takes place at a very low mean photon occupation of n_d ~ 3×10^{-4}. The onset of mechanical instability coincides with the blue-detuned region of the transition frequency ω_+ and ω_-, similar to the situation in the linear cavity optomechanics. As pump power is increased, the mechanical instability emerges near the higher transition frequencies around $\omega_{-\beta}$, and possibly around $\omega_{-\alpha}$ or $\omega_{+\beta}$. With further increases in the pump power, we observe instabilities near the bare cavity frequency. Surprisingly, we do not see any instability branch surrounding the transition frequency $\omega_{+\gamma}$. We also note that unstable mechanical response resulting in frequency comb features in PSD persist even beyond −5 dBm pump power. At these powers, we expect transmon to be ionized, and SQUID would operate in a non-zero voltage regime[31]. Due to the decoupling of the transmon mode, the transmission shows the bare cavity response, as shown in the lower panel of Fig. 5b.

Figure 5c shows similar measurements but at a different flux-operating point, such that the transmon qubit is approximately 240 MHz detuned above the cavity frequency. An instability region corresponding to single-photon transitions with frequency $\omega_{-\beta}$ and $\omega_{+\gamma}$ emerges, along with the instability branches surrounding the frequencies ω_+ and ω_-. At moderately higher power, the instability region near the two-photon transition corresponding to frequency $\omega_\gamma/2$ can be seen. We also observe the super-splitting of the ω_- peak, resulting in an abrupt widening of the instability region.

Semiclassical analysis and a model based on a quantum two-level system

To gain insight into these observations, we plot the transmission measurements $|S_{21}|$ over a large frequency at $B^{\parallel} = 0$ and the boundary of instability, together as shown in Fig. 6a. The instability parameter-space can be divided into three regions—(i) the low-power region, where the single-photon instabilities stem from the lower transitions, (ii) the mid-power region, where higher energy single- and multi-photon transitions, super-splitting, bistability of the electromagnetic mode are important, and (iii) the ionization region, where the frequency-comb persists despite the SQUID operating in the non-zero voltage regime.

As the EM mode emerges from the strong coupling between the transmon and the cavity, we model it by expanding it using polariton eigenstates to capture the low-power behavior. Such an approach effectively breaks down the EM mode into independent two-level systems, which are longitudinally coupled to a mechanical resonator. Details of the model are included in the Supplementary Note 6. Results from these calculations are plotted in Fig. 6b. As expected, the theoretical model is able to capture the behavior at low pump powers, however, it does not capture the experimental observations at intermediate or high pump powers.

For intermediate powers, we expect the system to behave more classically. Therefore, we also attempt a model based on the semiclassical analysis while treating the transmon as an anharmonic

https://doi.org/10.1038/s41467-024-51499-z

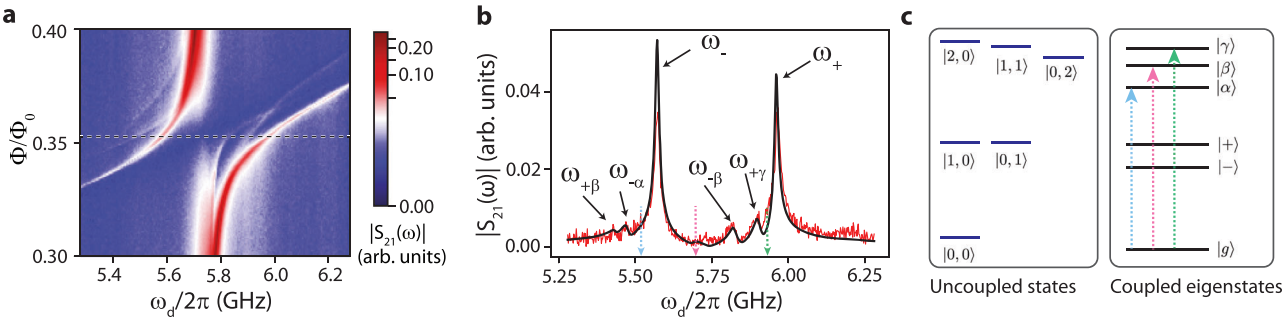

Fig. 4 | Higher-energy single-photon transitions of transmon-cavity system. a Colorplot showing the voltage transmission $|S_{21}(\omega)|$ through the cavity for Device-2 at relatively stronger probe. To suppress effects arising from the electromechanical interaction, no $B^{\parallel}$ is applied. **b** A linecut from $|S_{21}|$ measurement shown in panel (**a**) at the position shown by the dashed line. A small $B^{\perp}$ is used to tune transmon frequency while $B^{\parallel}$ is kept at zero. The solid line is the result of numerical calculations while considering a small thermal population in both transmon and cavity modes. Peaks are marked according to the transition frequencies. **c** Left panel shows the energy levels of uncoupled states of the transmon-cavity system. The right panel depicts energy eigenstates resulting from the strong coupling. The two-photon transitions are marked by colored arrows in (**b**) and (**c**).

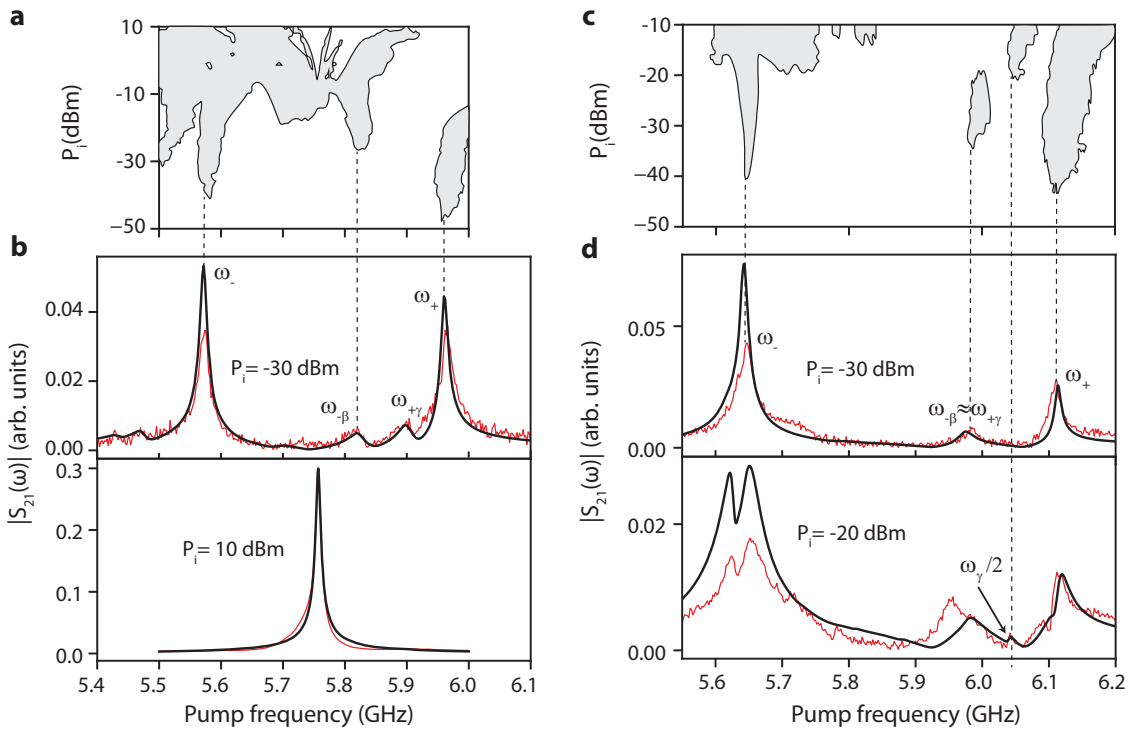

Fig. 5 | Mechanical instabilities due to single-, multi-photon transitions and super-splitted vacuum Rabi mode. a, **c** The regions of the mechanical instability in gray color as pump power P_i and frequency ω_d are varied. The measurements are carried out on Device-2 at two different flux bias points corresponding to $(\omega_q - \omega_c)/2\pi \sim 40$ MHz, and 240 MHz. **b**, **d** The transmission of the cavity for two different drive powers at $B^{\parallel} = 0$ mT. The black lines represent the results of the numerical calculations considering transmon's anharmonicity and treating it as a Kerr oscillator, except in the lower panel of (**b**) where the black line is a complex-Lorentzian fit of the transmission measurement. The numerical calculations capture the transition frequencies, however it does not capture the shape accurately presumably due to power dependent relaxation and dephasing rates of transmon. The dotted lines are drawn as a guide for the eye to connect to the instability onset points in panels (**a**, **c**).

oscillator (details are included in Supplementary Note 5). We first note that a driven transmon-cavity system alone (no optomechanical coupling) can have bistable and unstable solutions of the intra-cavity field[36]. We use a semi-classical approach and perform the linear stability test[37]. We identify the regions with one unstable fixed-point (FP), and regions with one unstable and two stable FP, as shown in Fig. 6c. In these regions, the intra-cavity field is expected to show either an unstable or a bistable behavior resulting in large photon-fluctuations.

Next, we include the optomechanical interaction, and obtain the fixed-points. The regions of the mechanical instability is shown by the dashed lines in Fig. 6c. At low powers, the semi-classical analysis could produce the mechanical instability region near the $\omega_{\pm}$ polaritons, arising from the optomechanical backaction. In addition, we note that in the optically bistable region, one of the stable solutions also give rise to mechanical instability.

Clearly, the quantum model based on the polariton-basis, and the three-mode semi-classical analysis do not capture the experimentally observed behavior completely. While the model based on the polariton-eigenstates captures the low-power behavior, it is not as effective in the mid-power range. Particularly, in the middle part of

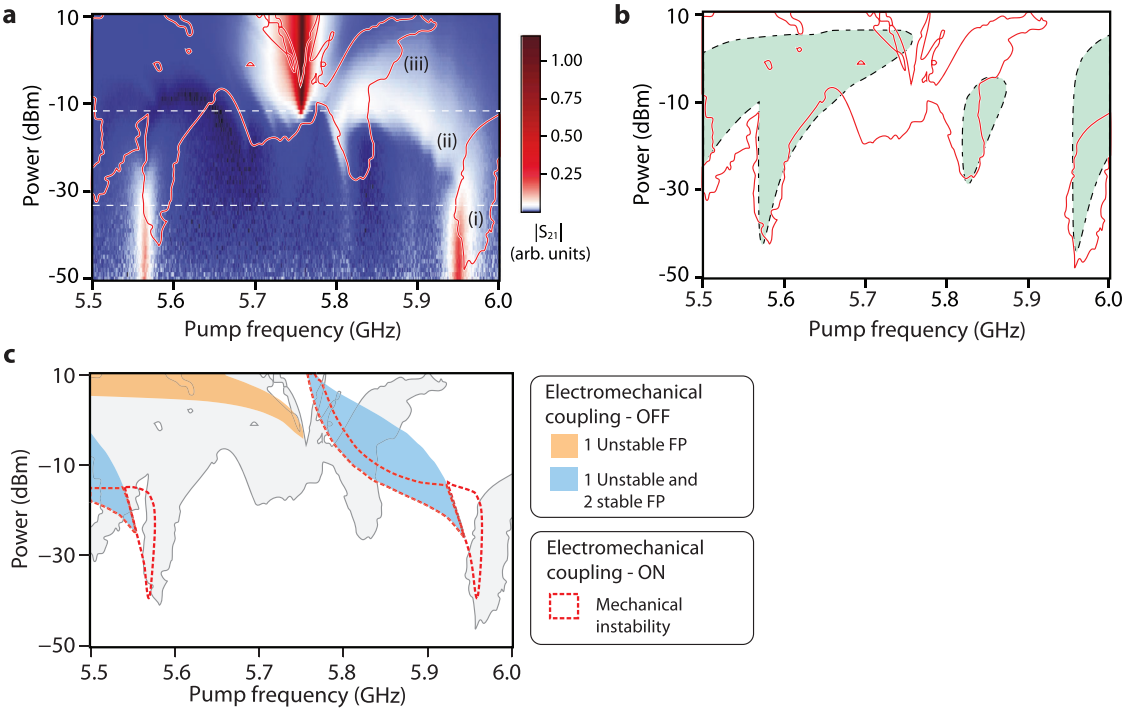

Fig. 6 | Insights into the instability region. a Transmission $|S_{21}(\omega)|$ of Device-2 as the pump power is varied. For a direct comparison with the various transitions relevant at high powers, the boundary of the instability region (as shown in Fig. 5a) is plotted on the top (red curve). **b** The region with a light green color shows the mechanical instability computed by modeling the electromagnetic mode using polariton eigenstates while considering their individual coupling to the mechanical mode with varying strengths. For comparison, the boundary of the instability is replotted (red curve). Panel **c** summarizes the results from a semi-classical analysis of the system. It shows different regions with one or more stable and unstable FP when the optomechanical coupling is set to zero. Region of mechanical instability due to optomechanical backaction for the stable FPs of the system is also included. The experimental boundary of mechanical instability is plotted in a light-gray color.

the region (ii), the transmon-cavity system undergoes a dissipative phase transition and can take a long time to reach equilibrium[23,28,30]. In this region, the presence of an unstable response in the experimental data, and the absence of it in the modeled results strongly suggest the role of fluctuating photon pressure on the mechanical resonator during the transition. These observations would require theoretical investigations beyond the standard semi-classical or two-level approach[38].

Discussion

To summarize our findings, our current experiment reaches a single-photon coupling rate which is nearly 4% of the mechanical resonator frequency. It highlights that instabilities arising from the residual thermal occupations of the mechanical and EM modes would become important as one reaches the single-photon strong coupling regime $g_0 \gtrsim \{\kappa, \omega_m\}$ unless the mechanical oscillator is cooled to its quantum ground state. Single-photon strong coupling regimes seem experimentally feasible as transmon qubits have been shown to operate in higher magnetic fields[32].

By changing the dimensions of the mechanical resonator and operating it in a higher magnetic field, it is feasible to achieve ground-state cooling via sideband driving below the level of a single photon. This also suggests ways to prepare non-classical mechanical states, including Schrödinger-cat states[21,22,39]. Such methods and techniques can be extended to the low-frequency flux-family superconducting qubits to realize transverse electromechanical couplings, thus extending the toolbox available with the flux-coupled devices[40]. The generation of microwave frequency combs at the single-photon level could have applications in quantum sensing[41,42]. Our experimental observations further demand theoretical investigation into the parametric instabilities in single photon limit.

Methods

The coaxial cavity is machined from oxygen-free high-conductivity copper. The central post (solid cylinder in the lower half) has a length of 11.5 mm and a diameter of 2.5 mm. The inner diameter of the outer cylinder is 5.5 mm, and the total height of the cavity is 20.5 mm. The transmon qubit is fabricated on an intrinsic silicon-(100) substrate. Using EBL and shadow evaporation of aluminum, we fabricate the device using a single step of lithography. The evaporated aluminum film is annealed under ambient conditions to transform the compressive stress into tensile stress. Selective etching of silicon is then carried out to release the nanowire (mechanical oscillator) from the substrate. To nullify the effects of annealing and etching on Josephson junction inductance, the oxidation parameter is tuned accordingly at the time of deposition so that we get the desired junction resistance at the end of all processes. Finally, the silicon chip is mounted inside the coaxial cavity and the cavity is placed inside a home-built vector magnet setup. This assembly is placed inside a double layer of infrared and magnetic field shields and mounted to the mixing chamber plate for cooling down to 20 mK for measurements.

Data availability

All the datasets used in this study are available in the Zenodo.

Code availability

The codes of this study are available from the corresponding authors upon request.

References

1. Aspelmeyer, M., Kippenberg, T. J. & Marquardt, F. Cavity optomechanics. *Rev. Mod. Phys.* **86**, 1391–1452 (2014).
2. Qiao, H. et al. Splitting phonons: building a platform for linear mechanical quantum computing. *Science* **380**, 1030–1033 (2023).

3. Bild, M. et al. Schrödinger cat states of a 16 microgram mechanical oscillator. *Science* **380**, 274–278 (2023).
4. Clerk, A. A., Lehnert, K. W., Bertet, P., Petta, J. R. & Nakamura, Y. Hybrid quantum systems with circuit quantum electrodynamics. *Nat. Phys.* **16**, 257–267 (2020).
5. Wollman, E. E. et al. Quantum squeezing of motion in a mechanical resonator. *Science* **349**, 952–955 (2015).
6. Pirkkalainen, J.-M., Damskägg, E., Brandt, M., Massel, F. & Sillanpää, M. A. Squeezing of quantum noise of motion in a micromechanical resonator. *Phys. Rev. Lett.* **115**, 243601 (2015).
7. Lecocq, F., Clark, J. B., Simmonds, R. W., Aumentado, J. & Teufel, J. D. Quantum nondemolition measurement of a nonclassical state of a massive object. *Phys. Rev. X* **5**, 041037 (2015).
8. Mason, D., Chen, J., Rossi, M., Tsaturyan, Y. & Schliesser, A. Continuous force and displacement measurement below the standard quantum limit. *Nat. Phys.* **15**, 745–749 (2019).
9. Peterson, G. A. et al. Ultrastrong parametric coupling between a superconducting cavity and a mechanical resonator. *Phys. Rev. Lett.* **123**, 247701 (2019).
10. Kotler, S. et al. Direct observation of deterministic macroscopic entanglement. *Science* **372**, 622–625 (2021).
11. Wollack, E. A. et al. Quantum state preparation and tomography of entangled mechanical resonators. *Nature* **604**, 463–467 (2022).
12. Seis, Y. et al. Ground state cooling of an ultracoherent electromechanical system. *Nat. Commun.* **13**, 1507 (2022).
13. Das, S. R. et al. Instabilities near ultrastrong coupling in a microwave optomechanical cavity. *Phys. Rev. Lett.* **131**, 067001 (2023).
14. Rodrigues, I. C., Bothner, D. & Steele, G. A. Coupling microwave photons to a mechanical resonator using quantum interference. *Nat. Commun.* **10**, 5359 (2019).
15. Bera, T., Majumder, S., Sahu, SudhirKumar & Singh, V. Large flux-mediated coupling in hybrid electromechanical system with a transmon qubit. *Commun. Phys.* **4**, 12 (2021).
16. Schmidt, P. et al. Sideband-resolved resonator electromechanics based on a nonlinear Josephson inductance probed on the single-photon level. *Commun. Phys.* **3**, 1–7 (2020).
17. Zoepfl, D., Juan, M. L., Schneider, C. M. F. & Kirchmair, G. Single-photon cooling in microwave magnetomechanics. *Phys. Rev. Lett.* **125**, 023601 (2020).
18. Bothner, D., Rodrigues, I. C. & Steele, G. A. Four-wave-cooling to the single phonon level in Kerr optomechanics. *Commun. Phys.* **5**, 33 (2022).
19. Zoepfl, D. et al. Kerr enhanced backaction cooling in magnetomechanics. *Phys. Rev. Lett.* **130**, 033601 (2023).
20. Via, G., Kirchmair, G. & Romero-Isart, O. Strong single-photon coupling in superconducting quantum magnetomechanics. *Phys. Rev. Lett.* **114**, 143602 (2015).
21. Khosla, K. E., Vanner, M. R., Ares, N. & Laird, E. A. Displacemon electromechanics: how to detect quantum interference in a nanomechanical resonator. *Phys. Rev. X* **8**, 021052 (2018).
22. Kounalakis, M., Blanter, Y. M. & Steele, G. A. Flux-mediated optomechanics with a transmon qubit in the single-photon ultrastrong-coupling regime. *Phys. Rev. Res.* **2**, 023335 (2020).
23. Chen, Qi-Ming et al. Quantum behavior of the Duffing oscillator at the dissipative phase transition. *Nat. Commun.* **14**, 2896 (2023).
24. Arcizet, O., Cohadon, P.-F., Briant, T., Pinard, M. & Heidmann, A. Radiation-pressure cooling and optomechanical instability of a micromirror. *Nature* **444**, 71–74 (2006).
25. Bishop, L. S. et al. Nonlinear response of the vacuum Rabi resonance. *Nat. Phys.* **5**, 105–109 (2009).
26. Bishop, L. S., Ginossar, E. & Girvin, S. M. Response of the strongly driven Jaynes-Cummings oscillator. *Phys. Rev. Lett.* **105**, 100505 (2010).
27. Shamailov, S. S., Parkins, A. S., Collett, M. J. & Carmichael, H. J. Multi-photon blockade and dressing of the dressed states. *Opt. Commun.* **283**, 766–772 (2010).
28. Brookes, P. et al. Critical slowing down in circuit quantum electrodynamics. *Sci. Adv.* **7**, eabe9492 (2021).
29. Fink, J. M., Dombi, A., Vukics, A., Wallraff, A. & Domokos, P. Observation of the photon-blockade breakdown phase transition. *Phys. Rev. X* **7**, 011012 (2017).
30. Sett, R. et al. Emergent macroscopic bistability induced by a single superconducting qubit. *PRX Quantum* **5**, 010327 (2024).
31. Shillito, R. et al. Dynamics of transmon ionization. *Phys. Rev. Appl.* **18**, 034031 (2022).
32. Krause, J. et al. Magnetic field resilience of three-dimensional transmons with thin-film Al/AlO x/Al Josephson junctions approaching 1 T. *Phys. Rev. Appl.* **17**, 034032 (2022).
33. Fleischhauer, M., Imamoglu, A. & Marangos, J. P. Electromagnetically induced transparency: optics in coherent media. *Rev. Mod. Phys.* **77**, 633–673 (2005).
34. Weis, S. et al. Optomechanically induced transparency. *Science* **330**, 1520–1523 (2010).
35. Agarwal, G. S. & Huang, S. Electromagnetically induced transparency in mechanical effects of light. *Phys. Rev. A* **81**, 041803 (2010).
36. Khan, S. & Türeci, H. E. Frequency combs in a lumped-element Josephson-junction circuit. *Phys. Rev. Lett.* **120**, 153601 (2018).
37. Strogatz, S. H. *Nonlinear Dynamics and Chaos: With Applications to Physics, Biology, Chemistry, and Engineering*, 2nd ed. (CRC Press, 2019) https://doi.org/10.1201/9780429492563.
38. Minganti, F., Biella, A., Bartolo, N. & Ciuti, C. Spectral theory of Liouvillians for dissipative phase transitions. *Phys. Rev. A* **98**, 042118 (2018).
39. Li, J., Gröblacher, S., Zhu, Shi-Yao & Agarwal, G. S. Generation and detection of non-Gaussian phonon-added coherent states in optomechanical systems. *Phys. Rev. A* **98**, 011801 (2018).
40. Najera-Santos, B.-L. et al. High-sensitivity ac-charge detection with a MHz-frequency fluxonium qubit. *Phys. Rev. X* **14**, 011007 (2024).
41. Di Candia, R., Minganti, F., Petrovnin, K. V., Paraoanu, G. S. & Felicetti, S. Critical parametric quantum sensing. *npj Quantum Inf.* **9**, 1–9 (2023).
42. Tang, Shao-Bo et al. Enhancement of quantum sensing in a cavity-optomechanical system around the quantum critical point. *Phys. Rev. A* **108**, 053514 (2023).

Acknowledgements

T.B. thanks Bhoomika Bhat, Harsh Vardhan Upadhyay and S. Majumder for assisting during the device fabrication and helpful discussions. This work is supported by the Air Force Office of Scientific Research under Award No. FA2386-20-1-4003. G.S.A. thanks the Infosys Foundation Chair of the Department of Physics, IISc Bangalore, which made this collaboration possible, and the AFOSR award no FA-9550-20-1-0366 for the support. The authors acknowledge the support under the CoE-QT by MEITY and the QuEST program by DST, Govt. of India. The authors acknowledge device fabrication facilities at CeNSE, IISc Bangalore, and central facilities at the Department of Physics funded by DST (Govt. of India).

Author contributions

V.S. conceived and supervised the experiment. T.B. fabricated the device and performed the measurements. T.B. and V.S. have done the data analysis. T.B., M.K., and G.S.A. carried out the theoretical calculations. All the authors have contributed to preparing the paper.

Competing interests

The authors declare no competing interests.

Additional information

Supplementary information The online version contains supplementary material available at https://doi.org/10.1038/s41467-024-51499-z.

Correspondence and requests for materials should be addressed to Tanmoy Bera or Vibhor Singh.

Peer review information *Nature Communications* thanks Qi-Ming Chen, Mathieu Juan and the other, anonymous, reviewer(s) for their contribution to the peer review of this work. A peer review file is available.